© 2021. Published by The Company of Biologists Ltd | Journal of Cell Science (2021) 134, jcs252197. doi:10.1242/jcs.252197

RESEARCH ARTICLE

Super-resolution microscopy reveals the arrangement of inner membrane protein complexes in mammalian mitochondria

Catherine S. Palmer[1], Jieqiong Lou[1,2], Betty Kouskousis[3,4], Elvis Pandzic[5], Alexander J. Anderson[1], Yilin Kang[1], Elizabeth Hinde[1,2] and Diana Stojanovski[1,*]

ABSTRACT

The mitochondrial inner membrane is a protein-rich environment containing large multimeric complexes, including complexes of the mitochondrial electron transport chain, mitochondrial translocases and quality control machineries. Although the inner membrane is highly proteinaceous, with 40-60% of all mitochondrial proteins localised to this compartment, little is known about the spatial distribution and organisation of complexes in this environment. We set out to survey the arrangement of inner membrane complexes using stochastic optical reconstruction microscopy (STORM). We reveal that subunits of the TIM23 complex, TIM23 and TIM44 (also known as TIMM23 and TIMM44, respectively), and the complex IV subunit COXIV, form organised clusters and show properties distinct from the outer membrane protein TOM20 (also known as TOMM20). Density based cluster analysis indicated a bimodal distribution of TIM44 that is distinct from TIM23, suggesting distinct TIM23 subcomplexes. COXIV is arranged in larger clusters that are disrupted upon disruption of complex IV assembly. Thus, STORM super-resolution microscopy is a powerful tool for examining the nanoscale distribution of mitochondrial inner membrane complexes, providing a 'visual' approach for obtaining pivotal information on how mitochondrial complexes exist in a cellular context.

KEY WORDS: Mitochondria, STORM, Nanoscopy, Mitochondrial complexes, Protein import, TIM23, COXIV

INTRODUCTION

Mitochondria are essential for eukaryotic cellular function, with central roles in cellular metabolism, energy production, calcium homeostasis and apoptosis, to name a few (Anderson et al., 2019; Nunnari and Suomalainen, 2012; Rossi et al., 2019). The mitochondrion is comprised of four compartments; the outer and the inner membranes, and the aqueous compartments comprising the intermembrane space and the matrix. The inner membrane is highly folded to increase the surface area for the production of energy and metabolites, with increased cristae density found in the mitochondria of cells with a high energy demand (Kühlbrandt, 2015; Mannella et al., 2013; Zick et al., 2009). The inner mitochondrial membrane is highly proteinaceous, with 40-60% of all mitochondrial proteins localised to this compartment (Morgenstern et al., 2017; Vögtle et al., 2017). This membrane contains a number of large multimeric membrane complexes, including the inner membrane protein translocase complexes like the translocase of the inner membrane 23 (TIM23 complex), complexes I–IV of the respiratory chain, and the protein scaffold MICOS (mitochondrial contact site and cristae organising system) (Kang et al., 2018; Kühlbrandt, 2015; Lobo-Jarne and Ugalde, 2018; van der Laan et al., 2016).

Import of nuclear-encoded mitochondrial precursor proteins is accommodated by large and dynamic multimeric machines, referred to as translocases. The translocase of the outer membrane (TOM) complex is a highly conserved multimeric machine that accommodates mitochondrial precursors as they passage across the outer membrane (Kang et al., 2018; Suzuki et al., 2000). The TIM23 complex mediates precursor import across or into the inner membrane (Kang et al., 2018). TIM23 is a versatile nanomachine, existing in different conformations that modulate the import of distinct classes of precursor proteins (Jackson et al., 2018; Mokranjac and Neupert, 2010). The association of a TIM23 'core' complex (consisting of TIM23, TIM50 and TIM17A/B, also known as TIMM23, TIMM50 and TIMM17A/B, respectively) (Jackson et al., 2018; Kang et al., 2018; Mick et al., 2012; Sinha et al., 2014) with the presequence-associated motor (PAM) gives rise to the $TIM23^{MOTOR}$ complex that facilitates precursor import into the mitochondrial matrix (Chacinska et al., 2005, 2010; Hutu et al., 2008). The PAM module contains multiple subunits, including mtHsp70, TIM44 (also known as TIMM44), GRPE1, Mortalin, MAGMAS (also known as PAM16) and DNAJC15/19 (Chacinska et al., 2009; Jackson et al., 2018; Kang et al., 1990, 2018; Mokranjac and Neupert, 2010; Naylor et al., 1998). Conversely, the addition of TIM21 and ROMO1 to the TIM23 core complex gives rise to the $TIM23^{SORT}$ complex, which facilitates the lateral insertion of precursor proteins into the inner membrane (Chacinska et al., 2009; Jackson et al., 2018; Kang et al., 2018). TIM21 is also involved in the assembly of complex IV subunits, connecting TIM23 to the biogenesis of the electron transport chain (ETC) (Mick et al., 2012). Complex IV (Cytochrome *c* oxidase or COX) is the final enzyme in the ETC, which catalyses the transfer of electrons from cytochrome *c* and the reduction of oxygen, and is coupled to the proton gradient (Kadenbach and Hüttemann, 2015; Zhao et al., 2019). Complex IV is assembled via modules with the use of multiple assembly factors, and the mature complex can be found in association with respiratory chain supercomplexes. The mitochondrial respiratory chain has been shown to exist in a number of forms within the mitochondrial inner membrane, with both a megacomplex ($MCI_2III_2IV_2$) and a supercomplex ($SCI_1III_2IV_1$) purified from mammalian cells

[1]Department of Biochemistry and Pharmacology and The Bio21 Molecular Science and Biotechnology Institute, The University of Melbourne, Parkville, Victoria 3010, Australia. [2]School of Physics, The University of Melbourne, Parkville, Victoria 3010, Australia. [3]Macfarlane Burnet Institute for Medical Research and Public Health, Melbourne, Victoria 3004, Australia. [4]Monash Micro Imaging, Monash University, Clayton, Victoria 3168, Australia. [5]Biomedical Imaging Facility, Mark Wainwright Analytical Centre, University of New South Wales, Sydney, NSW 2052, Australia.

*Author for correspondence (d.stojanovski@unimelb.edu.au)

D.S., 0000-0002-0199-3222

Handling Editor: Jennifer Lippincott-Schwartz
Received 27 July 2020; Accepted 3 June 2021

Journal of Cell Science (2021) 134, jcs252197. doi:10.1242/jcs.252197

(Gu et al., 2016; Guo et al., 2017). In addition, complex IV has been observed in smaller forms, as visualised by blue-native PAGE (BN-PAGE), including $CIII_2CIV$ and monomeric CIV (Lazarou et al., 2009; Schäfer et al., 2006).

Within the highly protein rich environment of the mitochondrial inner membrane, the spatial arrangement of large protein complexes has remained unclear. In part, this is because the average diameter of many mitochondrial protein complexes are well below the diffraction limit of optical microscopy, and thus much of what we know about the composition, activity and structural arrangement of the multimeric assemblies in mitochondria has come from biochemical studies. However, with the advent of super-resolution microscopy, visual insights into the nanoscale distribution of mitochondrial protein complexes have begun to emerge. For example, super-resolution technologies, such as stimulated emission depletion (STED) microscopy, and single molecule localisation microscopy (SMLM) methods, such as photoactivation localisation microscopy (PALM), have been used to investigate a variety of proteins in human mitochondria, including mitochondrial DNA arrangement, F_0F_1-ATP synthase and Bax assembly at the mitochondrial outer membrane (Brown et al., 2011; Dlasková et al., 2018; Jans et al., 2013; Klotzsch et al., 2015; Kukat et al., 2011; Salvador-Gallego et al., 2016; van de Linde et al., 2008; Wilkens et al., 2013). STED microscopy has shown that the inner membrane organising system (MICOS) is arranged in clusters at cristae junctions (Jans et al., 2013), and that a protein scaffold containing Mic60 (also known as IMMT) can form a helical arrangement in cristae of both yeast and human mitochondria (Stoldt et al., 2019). Furthermore, using STED, TOM20 (also known as TOMM20), a TOM receptor, was shown to be localised to clustered regions in the mitochondrial outer-membrane, forming a gradient distribution within the mitochondrial network that changes in response to growth conditions (Huang et al., 2008a; Wurm et al., 2011). The spatial arrangement of complex III and complex IV of the ETC have also been shown by immunoelectron microscopy to dynamically rearrange during assembly in yeast, with the localisation of subcomplexes found to be in distinct regions in the cristae (Stoldt et al., 2018). Furthermore, single-particle tracking and photoactivated localisation microscopy (SPT/PALM) has demonstrated the restricted diffusion of respiratory chain complexes in contrast to the more mobile outer-membrane components TOM20 and hFis1, and TIM23, which had restricted movement in mammalian cells (Appelhans and Busch, 2017; Appelhans et al., 2012; Salewskij et al., 2020; Wilkens et al., 2013).

Stochastic optical reconstruction microscopy (STORM) is a SMLM-based technique that detects photon emissions from single spatiotemporally distinct fluorescent molecules to precisely localise individual fluorophores and reconstruct a super-resolved image (Bates et al., 2007, 2013; Heilemann et al., 2008; Huang et al., 2008b; Rust et al., 2006). A cluster-based analysis of the fluorescently tagged protein positions within the many thousands of frames that make up a reconstructed STORM image enables extraction of the nanoscale organisation of proteins and protein complexes. This analysis segments the point localisation data into groups, in which a point is assigned to a cluster when it is in close proximity to many points from that cluster (Pageon et al., 2016a,b). Here, we couple N-STORM (Nikon STORM) with a density-based spatial clustering of applications with noise (DBSCAN) analysis to characterise the spatial organisation of mitochondrial inner membrane proteins TIM44, TIM23 and COXIV, alongside the outer membrane protein TOM20, in human mitochondria, and describe for the first time the cluster arrangement of mitochondrial inner membrane import proteins (Ester et al., 1996; Pageon et al., 2016a,b). This analysis showed that subunits of the TIM23 core complex (TIM23), PAM complex (TIM44) and complex IV (COXIV) of the ETC adopt unique spatial arrangements. The data indicate that different subcomplexes contain TIM23 or TIM44, as shown by cluster analysis, and a high number of clusters of TOM20 are indicative of the central role of the TOM complex in mitochondrial import. Furthermore, using a cell model of complex IV disassembly ($hTim8a^{KO}$ and $hTim8b^{KO}$ cells) (Kang et al., 2019), we showcase a change in the cluster dimensions of COXIV that is underpinned by an increase in molecule number per μm^2 and the number of clusters per μm^2, whereas the density of clusters is reduced in the $hTim8b^{KO}$. Therefore, N-STORM represents an invaluable method for analysing the spatial arrangement of mitochondrial membrane complexes and investigating how these complexes change in response to physiological cues.

RESULTS

Super-resolution microscopy reveals that human mitochondrial inner membrane proteins TIM23, TIM44 and COXIV are arranged in ordered clusters

Visualisation of mitochondrial translocases in the mitochondrial membrane has been limited by the spatial resolution of conventional fluorescence microscopy. The protein to lipid ratio within the mitochondrial inner membrane demonstrates the highly protein-rich environment, with almost half of the hydrophobic environment of the membrane taken up by protein (Schlame, 2021). Within the highly folded mitochondrial inner membrane, this protein crowding results in an estimated average surface distance of less than 10 nm between membrane proteins (Schlame, 2021). Given the size of mitochondrial membrane complexes (~16 nm by 10 nm, TIM22 complex; 13 nm by 10 nm, core TOM complex; 30 nm by 19 nm, respiratory super-complex $SCI_1III_2IV_1$) are well below the diffraction limit (~250 nm), and the protein-rich environment in which these complexes are found, optical microscopy alone is unable to provide quantitative information on the spatial arrangement of these multimeric assemblies within an intact mitochondrial membrane (Bausewein et al., 2017; Qi et al., 2021; Schlame, 2021; Wu et al., 2016). To overcome this limitation, we applied SMLM using N-STORM to achieve a localisation precision of ~20-30 nm to the TIM23 complex and complex IV, and then performed a DBSCAN analysis on the acquired datasets to extract quantitative information on how these mitochondrial proteins are clustered (Bates et al., 2007; Ester et al., 1996; Huang et al., 2008b; Rust et al., 2006). The use of DBSCAN allows analysis of the large datasets obtained by N-STORM, with 10,000 image frames collected per set, and the detection of arbitrarily shaped clusters rather than a bias to circular clusters (Ester et al., 1996). The advantage of STORM over other super-resolution microscopy techniques, such as SIM or STED, is the relatively simple and cost effective optical configuration, performed in total internal fluorescence (TIRF) mode here, which enables the barrier of diffraction limited imaging to be broken and subsequent cluster based analysis (Tam and Merino, 2015). In addition, with the combination of drift-corrected stable TIRF microscopy, STORM or other SMLM techniques, it is possible to achieve resolutions of a few nm (Coelho et al., 2020). We reasoned that the TIM23 complex and complex IV would be interesting candidates to analyse by N-STORM, as the TIM23 complex exists in two conformations: the $TIM23^{MOTOR}$ form with the PAM complex for matrix targeting of proteins; and the $TIM23^{SORT}$ complex (lacking PAM) for proteins destined for the inner membrane (Chacinska et al., 2005; Hutu et al.,

Journal of Cell Science (2021) 134, jcs252197. doi:10.1242/jcs.252197

2008; Mokranjac and Neupert, 2010). There is also a reported association with complex IV of the respiratory chain, with a member of the TIM23 complex implicated in the assembly of complex IV subunits (Mick et al., 2012).

HeLa cells were chemically fixed and immunodecorated with antibodies against the inner membrane translocase proteins TIM23 and TIM44, COXIV, as a component of complex IV, and TOM20, a TOM complex and outer membrane marker. The samples were analysed via both confocal and N-STORM microscopy. The submitochondrial localisation of TIM23, TIM44, TOM20 and COXIV proteins is depicted in Fig. 1A. In cultured HeLa cells, mitochondria form a reticular network that radiates out from the nucleus and extends throughout the cell (Fig. 1B, top panel). As visualised by confocal imaging, TOM20 staining in the mitochondrial outer membrane appeared to be homogeneous, whereas super-resolution microscopy revealed a more punctate staining pattern (Fig. 1B, bottom panel), as seen previously (Tam et al., 2014; Wurm et al., 2011). Using conventional diffraction limited imaging, each of the mitochondrial proteins examined (TOM20, TIM23, TIM44 and COXIV) appeared to be distributed throughout the mitochondrial tubules, with the fluorescent signal of the inner membrane proteins TIM23, TIM44 and COXIV displaying regions of higher intensity, presumably due to their location within the dense cristae (Fig. 1D-F, left panels). Although TOM20 was clearly localised to the outer mitochondrial membrane with confocal imaging (Fig. 1B, top panel, and Fig. 1C), the nanoscale arrangement of this protein as visualised by N-STORM displayed a clustered arrangement, with some dispersion throughout the tubule (Fig. 1B, top panel, and Fig. 1C), likely due to the increased mobility of TOM20 in the outer membrane (Appelhans and Busch, 2017). This arrangement is similar to that seen for TOM20 by STED super-resolution microscopy (Wurm et al., 2011). In comparison to TOM20, N-STORM microscopy revealed that TIM23 (Fig. 1D, right panel), TIM44 (Fig. 1E, right panel) and COXIV (Fig. 1F, right panel) were frequently visualised as clusters along the mitochondrial tubule. These clusters were often observed to be at regular intervals (Fig. 1D,E) at opposite sides of the tubule (Fig. 1F), or in helical arrangements (Fig. 1F), which is indicative of mitochondrial inner membrane protein arrangement in the cristae, as recently shown with the mitochondrial inner membrane protein Mic60 using STED super-resolution microscopy (Stoldt et al., 2019). Owing to the compact nature of the perinuclear region of the mitochondrial network, these arrangements were most clearly seen in the peripheral tubules of the mitochondria.

TIM23 and TIM44 have distinct arrangements in the mitochondrial inner membrane

To quantify mitochondrial protein clusters in the mitochondrial network, we acquired N-STORM data in HeLa cells immunolabelled for the proteins TOM20, TIM23, TIM44 and COXIV. DBSCAN analysis was then applied to N-STORM SMLM point localisation data as a means to quantify the number of molecules and clusters in a region of interest, as well as the number of localisations per cluster and the cluster size (Fig. 2A). DBSCAN is a propagative cluster detection method that links points that are closely packed together, and which has been modified for N-STORM data analysis in a customised cluster detection analysis program (Clus-DoC) (Ester et al., 1996; Pageon et al., 2016a,b). We applied DBSCAN via Clus-DoC to N-STORM point localisation data obtained from three independent experiments; at least nine cells per protein were examined, from which ≥33 regions per condition were analysed. Using this analysis, clusters are identified as overlapping regions of high density separated by regions of low density, and, as such, allow the identification of clusters of different size, density and shape (Ester et al., 1996; Pageon et al., 2016a,b). TOM20 displayed the highest average number of clusters (10.27±4.47; mean±s.d.) per area (μm^2), whereas TIM23 displayed the lowest average number of clusters (4.82±1.66) per area (μm^2) (Fig. 2B). These results are also mirrored in the molecule density expressed as the number of molecules (per μm^2), with TOM20 displaying the highest and TIM23 the lowest average number of molecules (Fig. S1A). COXIV had the highest number of molecules detected per cluster, which is indicative of the abundance of the respiratory chain in mitochondria (Fig. S1B). Given that the TOM complex is the main entry gate for precursors into mitochondria, it would be expected that there are more TOM complex clusters, as detected by TOM20 (Bausewein et al., 2020). Indeed, a comprehensive proteomic analysis of isolated mitochondria showed that the TOM complex was the most abundant translocase, highlighting the importance of this complex in mitochondrial import (Morgenstern et al., 2017). Indeed, this was supported by fewer detected clusters of TIM23, which represents a downstream translocase for a subset of mitochondrial precursors. The largest variation in cluster number was observed in the number of TOM20 clusters per μm^2 (Fig. 2B), suggesting possible different conformations in which TOM20 is associated with the TOM complex during TOM complex biogenesis at early and late stages of complex assembly (Humphries et al., 2005; Model et al., 2001). Alternatively, this variation in cluster number may also be caused by dynamic or transient association of TOM20 with the core TOM complex, which may be disrupted upon chemical fixation (Suzuki et al., 2000). The large variation in the number of clusters of Tom20 per μm^2 also supports the model of increased fluidity of proteins in the outer membrane, as proteins move throughout different regions of the membrane (Appelhans and Busch, 2017). In addition, variation in the cluster density of TOM20 within mitochondria has been described previously, with the density of TOM20 higher in mitochondria adjacent to the nucleus compared to mitochondria at the periphery of the cell (Wurm et al., 2011). As such, the variation in TOM20 cluster number per μm^2 may be a result of the range of regions within the mitochondrial network analysed for each cell.

TIM23 and TIM44 have less variation in the average number of clusters per area compared to TOM20 and COXIV (Fig. 2B). Despite having a smaller number of clusters per μm^2 than the other proteins investigated here, TIM23 was found to have a significantly greater average cluster density than COXIV, TIM44 and TOM20 (Fig. 2B,C). Of note, TIM23 had significantly fewer clusters per μm^2 than TIM44 (Fig. 2B). This may be because of the dynamic nature of the TIM23 and the PAM complexes, which have been proposed to undergo multiple association and dissociation events (Chacinska et al., 2005; Popov-Čeleketić et al., 2008; van der Laan et al., 2007). Interestingly, TIM44 had the greatest average cluster area (nm^2) (Fig. 2D), but the lowest average relative cluster density (Fig. 2C). We note that a polyclonal TIM44 antibody was used, and the cluster density for this protein may be inflated. Additionally, the TIM44 distribution of cluster area was bimodal (Fig. 2D), providing evidence that TIM44 may exist in distinct subcomplexes. In support of this finding, dual colour N-STORM localisation of TIM23 and TIM44 indicated that the TIM23 complex is heterogenous within the mitochondrial inner membrane, with TOM20 and COXIV as controls (Fig. S2A,B). The arrangement of TIM23 and TIM44 in the mitochondrial inner membrane is likely to exist in multiple conformations depending on the status of protein import

Journal of Cell Science (2021) 134, jcs252197. doi:10.1242/jcs.252197

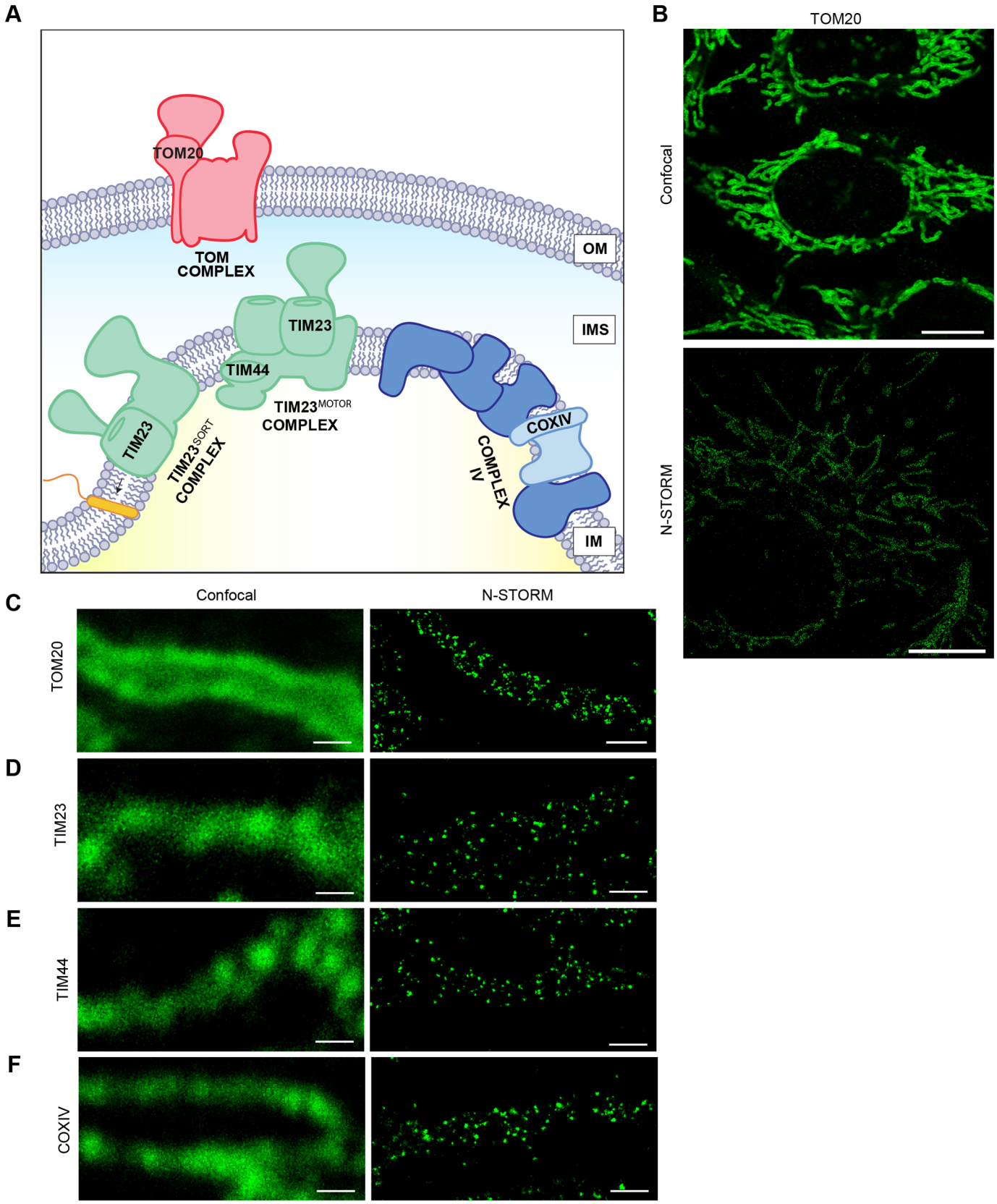

Fig. 1. See next page for legend.

(Chacinska et al., 2005, 2010; van der Laan et al., 2007). During active import of matrix-destined proteins, the PAM complex is recruited to the TIM23 complex in response to a signal cascade (Chacinska et al., 2005). It has been previously demonstrated that PAM components MAGMAS (yPam16) and DNAJC19 form a stable subcomplex in mammalian cells (Sinha et al., 2010). The data

Journal of Cell Science (2021) 134, jcs252197. doi:10.1242/jcs.252197

Fig. 1. The nanoscale distribution of TOM20, COXIV, TIM23 and TIM44 in mammalian cells. (A) Schematic of the submitochondrial localisation of TIM23, TIM44, TOM20 and COXIV proteins. TOM20 is associated with the TOM Complex in the outer mitochondrial membrane. TIM23 and TIM44 are components of the TIM23 complex in the inner membrane. COXIV is a subunit of complex IV of the respiratory chain (CIV) in the mitochondrial inner membrane. (B) HeLa cell immunostained for TOM20 showing a comparison of confocal microscopy (top) and reconstruction of N-STORM point localisation (bottom). (C-F) HeLa cells immunostained for TOM20 (C), TIM23 (D), TIM44 (E) and COXIV (F), and visualised by confocal microscopy (left) and reconstruction of N-STORM super-resolution point localisation (right). Scale bars: 10 µm (B); 0.5 µm (C-F).

featured in Fig. 2B support the biochemical data that human TIM44 exists in a subcomplex ready to associate with TIM23 upon activation via signal cascade, resulting in additional TIM44 clusters.

TIM44 and TOM20 had similar cluster densities, suggesting that although they may have a greater number of clusters present, they contain fewer proteins compared to TIM23 and COXIV (Fig. 2B,C). As can be observed from the cluster maps and quantification of the average cluster area (Fig. 2A,D), both COXIV and TIM44 formed large clusters in the membrane; however, TIM44 did have a greater spread in measurements than COXIV, similar to that observed for TOM20, indicating a variety in calculated cluster size (Fig. 2D). Together these data provide information on the nanoscale distribution of the mitochondrial complexes containing TIM23, TIM44, COXIV and TOM20. The mitochondrial distributions of TIM23 and TIM44 are consistent with them existing in a constrained conformation at the boundary membrane, with TIM44 existing in two distinct pools (Appelhans and Busch, 2017; Stoldt et al., 2019).

Loss of hTim8a or hTim8b alters COXIV distribution in the mitochondrial membrane

We wanted to ascertain whether we could use this visual approach to detect physiological changes to inner membrane complexes. Recently, Kang et al. (2019) showed that loss of the intermembrane space chaperone hTim8a or hTim8b resulted in cell line-specific changes in the protein levels and assembly of complex IV (Kang et al., 2019). Specifically, the amount of intact complex IV, as detected by the subunit COXIV on BN-PAGE, was decreased in HEK293 cells lacking Tim8b (Tim8b^{KO}); in addition an increase in a higher molecular complex was observed. A similar loss of complex IV on BN-PAGE was seen in SH-SY5Y cells lacking hTim8a (Kang et al., 2019). Although the stability of complex IV was shown to be affected upon loss of hTim8a or hTim8b, the protein level of the subunit COXIV was not affected (Kang et al., 2019). Subsequently, visualisation of COXIV nanoscale localisation in the mitochondrial inner membrane may provide unique insight into the effect of the loss of hTim8a or hTim8b on complex IV. We set out to assess the arrangement of COXIV protein in hTim8a^{KO} or hTim8b^{KO} HEK293 cells compared to control HEK293 cells to ascertain whether we could mirror these biochemically characterised changes using high resolution imaging. N-STORM reconstruction images were obtained for at least ten cells from three independent experiments for each cell line examined, from which ≥35 regions per condition were analysed using cluster analysis.

There were no observable differences in the fluorescence intensity of COXIV between control and hTim8a^{KO} or hTim8b^{KO} HEK293 cells, as visualised by confocal microscopy (Fig. 3A). In contrast, N-STORM microscopy revealed a change in the arrangement of COXIV in the mitochondrial tubule in both the hTim8a^{KO} and hTim8b^{KO} cells compared to control cells (Fig. 3A,B). Line scan analysis of the COXIV localisation profile in the hTim8a^{KO} and hTim8b^{KO} cells revealed a significantly greater number of COXIV intensity peaks in hTim8a^{KO} and hTim8b^{KO} HEK293 cells compared to wild-type cells (Fig. 3B,C), indicating increased frequency of COXIV points in these cells compared to wild-type HEK293 cells. In support of this, cluster analysis of N-STORM localisation data revealed a significant difference in the number of molecules per µm of both hTim8a^{KO} and hTim8b^{KO} mitochondria compared to control mitochondria (Fig. 4A,B); however, there was no significant difference between hTim8a^{KO} and hTim8b^{KO} HEK293 cells. hTim8b^{KO} mitochondria also exhibited a significantly greater number of clusters per µm^2 and relative cluster density when compared to hTim8a^{KO} and control cells (Fig. 4C,D). There was also a significant increase in the average cluster area (nm^2) in the hTim8a^{KO} cells compared to control cells (Fig. 4E). This indicates an alteration in the spatial arrangement of complex IV in hTim8a^{KO} HEK293 cells. The differences in complex IV assembly in HEK293 cells was also observed biochemically and indicates potential differences in the role of these proteins in the stability of complex IV (Kang et al., 2019). Interestingly, of the four DBSCAN parameters described here, the greatest change was observed in hTim8b^{KO} HEK293 cells compared to both wild-type and hTim8a HEK293 cells. This is in agreement with the biochemical results presented by Kang et al. (2019), with a significant change in complex IV stability on BN-PAGE observed in hTim8b^{KO} HEK293 cells but not hTim8a^{KO} HEK293 cells. The change in the cluster arrangement of COXIV in the hTim8a^{KO} and hTim8b^{KO} HEK293 cells provides a unique insight into the arrangement of complex IV in these cells once the complex has been destabilised. These possible subcomplexes containing COXIV are not visible with BN-PAGE analysis (Kang et al., 2019); however, it is possible that these subcomplexes are not stable and are subsequently lost following detergent solubilisation of samples, or consequently could be exclusively assembled into the respiratory chain super-complex in hTim8b^{KO} cells, as seen with the presence of the higher molecular weight complex visible with BN-PAGE (Kang et al., 2019). Based on the number of molecules detected within the COXIV clusters, this would represent a number of complex IV modules within this cluster in the form of super-complexes and/or the complex IV monomer and dimer, and could indicate regions within the inner membrane that are concentrated sites containing the respiratory chain complexes. In addition, the different effects of the loss of Tim8a or Tim8b in HEK293 cells indicates a possible role for these proteins at different stages of complex IV assembly.

These results demonstrate the additional information obtained from N-STORM microscopy and cluster analysis in cell models that was not available using biochemical analysis or conventional microscopy. Taken together, these data extend previous biochemical analysis of complex IV assembly in cells lacking hTim8a or hTim8b (Kang et al., 2019). Super-resolution microscopy has demonstrated that complex IV may indeed still be present; however, the COXIV protein is no longer maintained solely in clusters, as seen in control cells. DBSCAN analysis revealed that the number of clusters per µm^2 and the relative cluster density in hTim8b^{KO} cells were in fact affected when compared to control cells, with a significant difference in the number of molecules per µm for both knockout cells lines, providing new insight into the arrangement of complex IV upon changes to the complex stability in hTim8a^{KO} and Tim8b^{KO} HEK293 cells.

Journal of Cell Science (2021) 134, jcs252197. doi:10.1242/jcs.252197

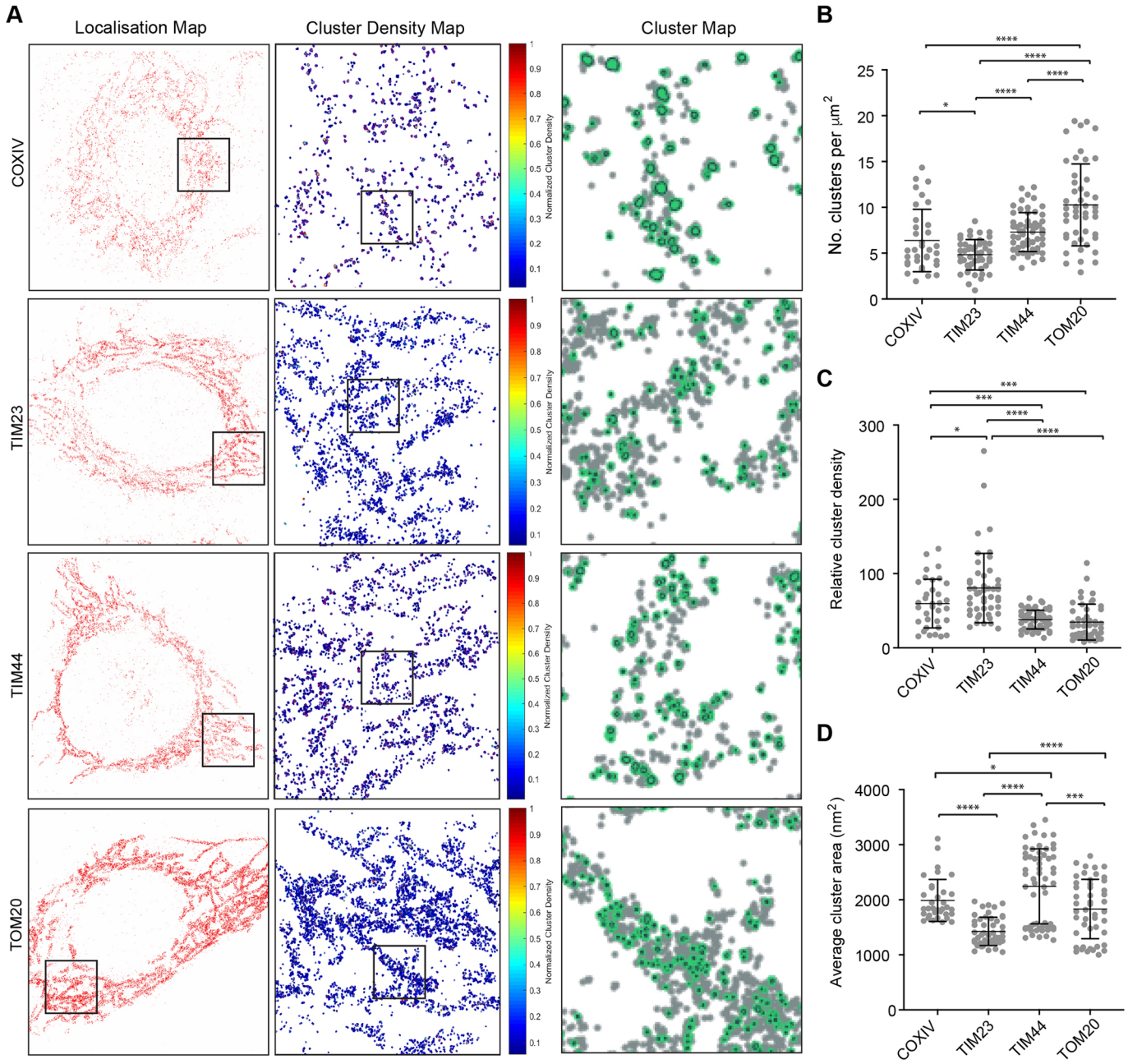

Fig. 2. Cluster analysis of TOM20, TIM23, TIM44 and COXIV single molecule localisation microscopy. (A) Representative reconstruction of single molecule localisation for COXIV, TIM23, TIM44 and TOM20 shown as a localisation map (left). Cluster density map from representative regions highlighted, corresponding to the left box (middle), highlighted in the cluster map regions corresponding to the middle box (right). Representative regions of 4×4 μm^2 were analysed for cluster properties. (B) Number of clusters per μm^2 of selected regions from single molecule localisation. (C) Relative cluster density of selected regions from single molecule localisation. (D) Average cluster area (nm^2) of selected regions from single molecule localisation. Cluster analysis was performed using DBSCAN. *n*=3 experiments, ≥33 regions from at least nine cells per protein examined. Data are mean±s.d.; **P*<0.05, ****P*<0.001, *****P*<0.0001 (unpaired *t*-test with Welch's correction).

DISCUSSION

We have used N-STORM super-resolution microscopy to visualise complexes of the mitochondrial inner membrane. Specifically, we show that two components of the TIM23 Complex, TIM23 and TIM44, form clusters within the mitochondrial inner membrane that exhibit distinct properties in terms of number, density and area (Fig. 2). In addition, these clusters exhibited an ordered rail-like arrangement as observed recently for Mic60 using STED super-resolution microscopy (Stoldt et al., 2019). Although the TIM23 complex has been studied extensively in yeast and mammalian cells using biochemical methods, there is little information on the nanoscale arrangement within the mitochondrial inner membrane. This represents, to our knowledge, the first study to explore the arrangement of this complex in the mitochondrial inner membrane using STORM microscopy. The similarity of the arrangement within the membrane to that observed with components of the MICOS complex (Stoldt et al., 2019) suggests that the TIM23 complex is localised to specific regions within the membrane, possibly at cristae junctions. TIM44 has been described to have a role in the recruitment of the J-complex (DNAJC19 and

Journal of Cell Science (2021) 134, jcs252197. doi:10.1242/jcs.252197

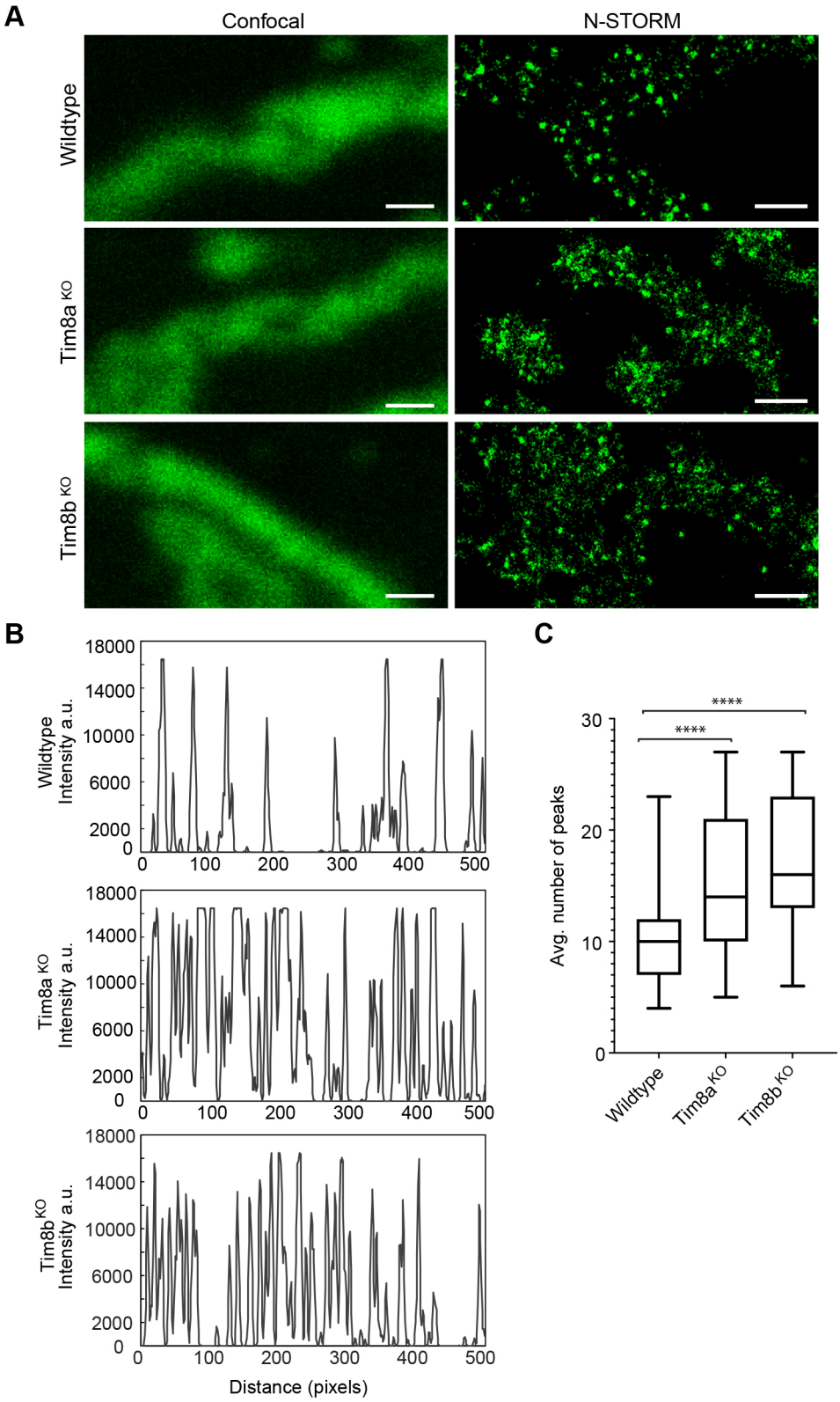

Fig. 3. COXIV localisation is dispersed in Tim8a^{KO} HEK293 and Tim8b^{KO} HEK293 cells compared to control cells. (A) Left: wild-type, Tim8a^{KO} and Tim8b^{KO} HEK293 cells immunostained for COXIV, and visualised by diffraction limited confocal microscopy. Right: reconstruction of STORM super-resolution microscopy point localisation. Scale bars: 0.5 µm. (B) Wild-type, Tim8a^{KO} and Tim8b^{KO} HEK293 cells immunostained for COXIV, and analysed by N-STORM super-resolution microscopy. Line scans from 2 µm regions were obtained using the Dynamic ROI profiler plugin in Fiji image analysis software. Example line scans are presented here. (C) The average number of peaks [>5000 arbitrary unit (a.u.) intensity] from 2 µm lines were recorded (n=3 experiments with ≥13 cells analysed, five regions per cell). Lower and upper box boundaries are the 25th and 75th percentiles, respectively, line inside box is median, upper and lower error lines are maximum and minimum, respectively. ****P<0.0001 (unpaired t-test with Welch's correction).

MAGMAS) to the TIM23 complex to facilitate translocation of the preprotein across the membrane, with DNAJC19 and MAGMAS forming a subcomplex in human cells (Hutu et al., 2008; Sinha et al., 2010). The TIM44 clusters described here indicate that TIM44 possibly exists in a subcomplex prior to associating with the TIM23^{CORE} during active import. As there are multiple forms of the TIM23 complex, it is plausible that subcomplexes are recruited to the TIM23^{CORE} upon a signal cascade to enable a rapid response to protein import. Alternatively, as TIM44 is a proposed scaffolding and recruiter for the PAM complex during active protein import, these two cluster populations may represent those engaged in active import and bound to the PAM complex, and those that are not

Journal of Cell Science (2021) 134, jcs252197. doi:10.1242/jcs.252197

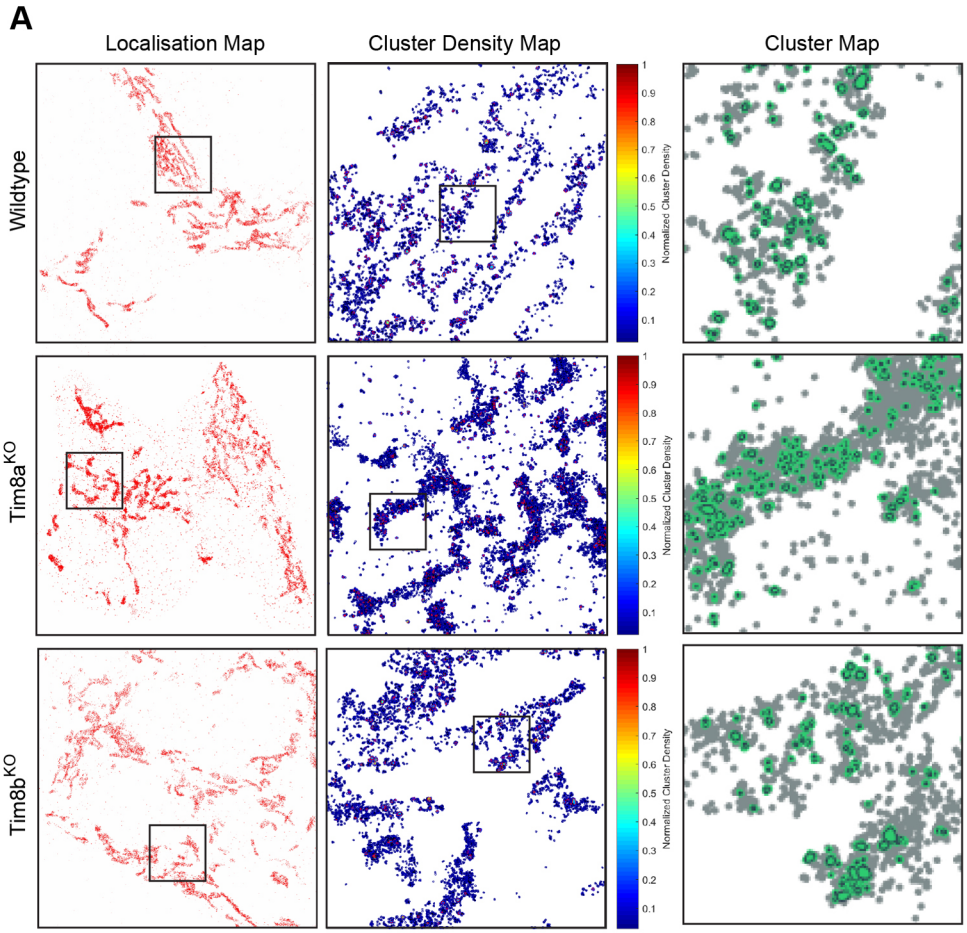

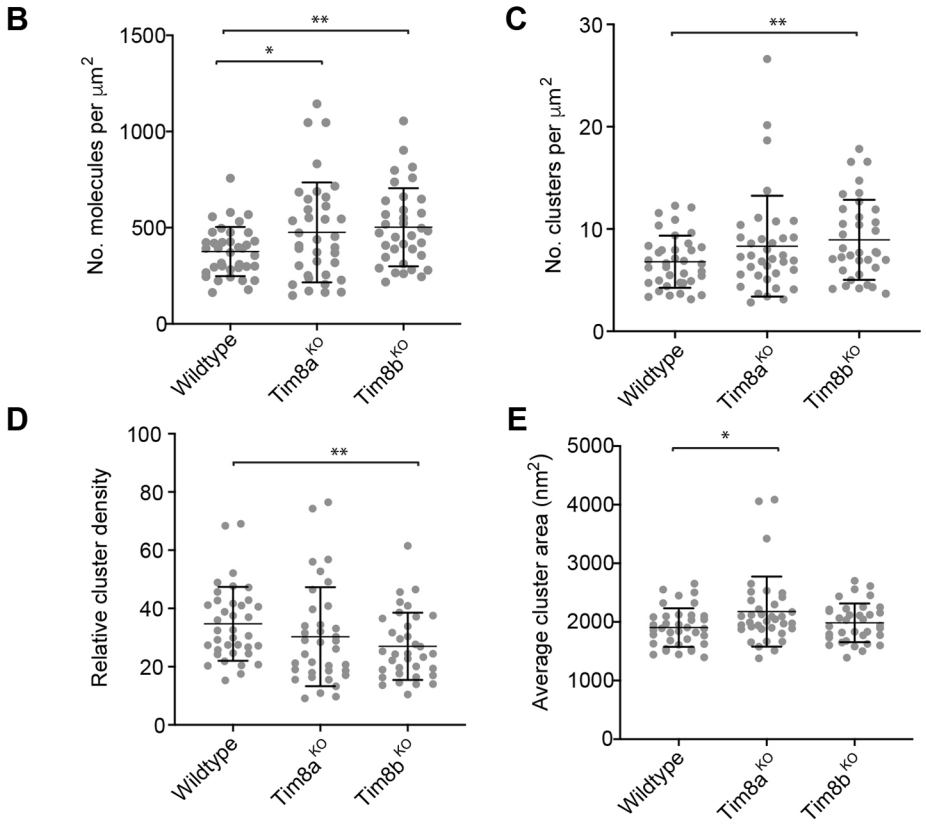

Fig. 4. Cluster analysis of COXIV single molecule localisation data in Tim8a^{KO}, Tim8b^{KO} and control HEK293 cells. (A) Representative reconstruction of single molecule localisation for COXIV in wild-type, Tim8a^{KO} and Tim8b^{KO} HEK293 shown as a localisation map (left). Cluster density map from representative regions highlighted, corresponding to the left box (middle), highlighted in the cluster map regions corresponding to the middle box (right). (B) Number of molecules per µm^2 of selected regions from single molecule localisation. (C) Number of clusters per µm^2 of selected regions from single molecule localisation. (D) Relative cluster density of selected regions from single molecule localisation. (E) Average cluster area of selected regions from single molecule localisation. Cluster analysis was performed using DBSCAN. n=3 experiments, ≥23 regions from at least five cells per cell line. Data are mean±s.d.; *P<0.05, **P<0.01 (unpaired t-test with Welch's correction).

(Chacinska et al., 2005, 2010; Hutu et al., 2008). Complementary biochemical analysis is required to investigate this further.

Using N-STORM super-resolution microscopy, we could look at a previously described system of complex IV disassembly and mirror these biochemical observations. We could describe the localisation of COXIV in cells lacking mitochondrial chaperones, but also demonstrate the use of nanoscale imaging in analysis of complex IV formation. The loss of hTim8a or hTim8b in HEK293 and SH-SY5Y cells causes a significant reduction in the complex IV copper chaperone COX17 (Kang et al., 2019). Reduction of COX17 has also been shown to reduce the level of correctly assembled respiratory chain super-complex without causing a reduction in the amount of the complex IV dimer, as detected by BN-PAGE (Oswald et al., 2009). Our data show that loss of hTim8b in HEK293 cells results in a change in the density and the number of clusters of COXIV within mitochondria, indicating a possible destabilisation of complex IV. Interestingly, the same phenotype was observed following the loss of hTim8a, despite a different profile of complex IV in HEK293 cells visible on BN-PAGE (Kang et al., 2019), demonstrating the novel information available from super-resolution microscopy. The loss of hTim8b in HEK293 cells also results in the reduction of the mitochondrial respiratory chain assembly factor HIGD2A, as shown by mass spectrometry analysis (Kang et al., 2019). This assembly factor was recently shown to affect supercomplex assembly and defective complex IV activity (Hock et al., 2020; Timón-Gómez et al., 2020). The loss of the complex IV assembly factors COA6 or HIGD2A has also recently been shown to result in a loss of the holo-complex IV, with a concurrent stabilization of complex IV-containing supercomplexes (Hock et al., 2020; Stroud et al., 2015). As such, the loss of Tim8b in HEK293 cells may result in a similar phenotype, as demonstrated by the higher molecular weight supercomplex visible on BN-PAGE (Kang et al., 2019). This analysis demonstrates that the stability of complex IV and/or association with the supercomplex can be detected supporting the role of the small TIM proteins in the biogenesis of complex IV.

These results demonstrate that N-STORM super-resolution microscopy is a powerful technique that can provide visualisation and quantification of mitochondrial inner membrane complexes. Future analysis of mitochondrial membrane complexes with N-STORM and DBSCAN analysis could include colocalisation analysis to examine complex formation in both control and deficient cell lines, providing unique insight into the formation of these complex machineries. In addition, super-resolution microscopy can give a unique insight into the fate of proteins and/or complexes upon physiological insults, such as cell death induction or cell cycle arrest.

MATERIALS AND METHODS

Cell culture

The cell lines used in this study were HeLa (kindly provided by Prof. Paul Gleeson, The University of Melbourne, Australia), HEK293 Flp-In (Thermo Fisher Scientific) and HEK293 Flp-In Tim8a^{KO} and HEK293 Flp-In Tim8b^{KO} cells. Tim8a^{KO} and Tim8b^{KO} cells were generated using CRISPR/Cas9-mediated gene editing (Kang et al., 2019). HeLa and parental HEK293 Flp-In cells have been verified by STR profiling, as described previously (Kang et al., 2017). Cells were routinely checked for mycoplasma contamination using a MycoAlert Mycoplasma detection kit (Lonza). Cells were cultured in Dulbecco's modified Eagle's medium (Gibco) containing 4.5 g/l glucose supplemented with 10% (v/v) foetal bovine serum (FBS, *In vitro* Technologies) and 0.01% penicillin-streptomycin (v/v) (Gibco), and cultured in an atmosphere of 5% CO^2 at 37°C.

Sample preparation

Cells were seeded onto Lab-Tek II Chambered coverglass (Thermo Fisher Scientific) chambers and grown for 1-3 days (37°C, 5% CO_2). For immunolabelling, cells were fixed with 4% paraformaldehyde (Proscitech) and 0.1% glutaraldehyde (Sigma-Aldrich) diluted in PBS [137 mM NaCl, 2.7 mM KCl, 10 mM Na_2HPO_4 and 1.8 mM KH_2PO_4, (pH 7.4)] containing 5% (w/v) sucrose (Sigma-Aldrich) for 10 min at room temperature. Following fixation, cells were washed with PBS and permeabilised with 0.1% (v/v) Triton X-100 (Sigma-Aldrich) in PBS, and subsequently blocked with 5% bovine serum albumin (w/v) in PBS for 1 h at room temperature. Primary antibodies used were directed against the proteins Tom20 (F10) (1:500, Santa Cruz Biotechnology, sc-11415, batch 2117), Tim23 (Clone 32) (1:300, BD Biosciences, 611222, batch 7208950), Tim44 (1:300, Proteintech, 13859-1-AP) and COXIV (3E11) (1:300, Cell Signaling Technology, 4850S, lot 10). For conventional imaging, goat anti-rabbit IgG Alexa Fluor 568 or goat anti-mouse IgG Alexa Fluor 488 (1:500, Thermo Fisher Scientific, Molecular Probes A11011, lot 2017252 and A11001, lot 2015565) secondary antibodies were used. For N-STORM imaging, primary antibodies were detected with custom dual-labelled secondary antibodies (1:100, anti-mouse Cy 2 Alexa Fluor 647, anti-mouse Cy 3 Alexa Fluor 647, anti-rabbit Cy 2 Alexa Fluor 647 and anti-rabbit Cy 3 Alexa Fluor 647). Customised secondary antibodies were generated using the dye pair Alexa Fluor 647 Carboxylic acid (A20006, Invitrogen) and Cy 3 mono-reactive dye (GE Healthcare, PA23001) or Cy 2 bis-reactive dye (GE Healthcare, PA22000), 1 M $NaHCO_3$ and AffiniPure donkey anti-rabbit IgG (Jackson ImmunoResearch Europe, 711-005-152, lot 136480) or AffiniPure donkey anti-mouse IgG (Jackson ImmunoResearch Europe, 715-005-151, lot 136584). Reagents were incubated for 30 min at room temperature, and subsequently purified using a NAP-5 gel filtration column (GE Healthcare, 17-0853-02). STORM imaging was conducted in a buffer containing 50 mM Tris (pH 8.0), 10 mM NaCl, 10% (w/v) glucose, 7 µl β-mercaptoethanol and 7 µl GLOX [56 µg/ml glucose oxidase, 3.4 µg/ml catalase, 10 mM Tris (pH 8.0) and 50 mM NaCl].

Fluorescence microscopy

Conventional imaging of cells was conducted using a Leica SP8 confocal microscope equipped with a 488 nm 20 mW solid-state laser and a direct modulation laser diode (DMOD) 405 nm 50 mW laser, and a SP PMT spectral fluorescence detector. Samples were mounted on a 63×/1.4 HC PL APO CS2 oil lens and images were captured using Leica LAS X SP8 software. Laser intensity and gain were optimized for each sample. Images were processed using Fiji image software (Schindelin et al., 2012).

N-STORM microscopy was conducted using a Nikon N-STORM microscope equipped with a TIRF objective. N-STORM microscopy was collected in a 256×256-pixel (156 nm/pixel) region of interest through a Nikon 100×/1.4 NA oil objective, with TIRF angle and focus adjusted to optimize signal to noise ratio. Cy 2 or Cy 3 and Alexa Fluor 647 fluorophores were excited with 488 nm or 561 nm and 647 nm laser lines, respectively, and recorded using an Andor EMCCD iXon3 or Andor EMCCD iXon DU897 camera. For each reconstruction, 10,000 frames were acquired (16 ms/frame exposure), and reconstruction was performed using Nikon NIS Elements N-STORM Software.

Image analysis

Line scan analysis was completed using the Dynamic ROI Profiler in Fiji (Schindelin et al., 2012). For each cell, 5×2 µm lines were performed. The number of peaks >5000 intensity (a.u.) was recorded for each 2 µm line. Measurements were obtained from ≥13 cells, five measurements per cell from three independent experiments. SMLM N-STORM data were analysed using custom software written in MATLAB (MathWorks) (Pageon et al., 2016a,b) for the detection of clusters and extraction of clustering parameters. Typically, for each cell, one to five non-overlapping representative regions of 4×4 µm^2 were selected for analysis. N-STORM data obtained from DBSCAN analysis was used to identify individual clusters. The DBSCAN method detects clusters using a propagative method that links points belonging to the same cluster based on two parameters; the minimum number of neighbours $\mathcal{E}$ ($\mathcal{E}$=3) in the radius of r (r=10 nm), and clusters had at least ten molecules. The DBSCAN routine was implemented

in MATLAB and subsequently coded in C++, and compiled in a MEX file (Pageon et al., 2016a). Statistical analysis was conducted using GraphPad Prism9. Significance was determined using an unpaired two-tailed *t*-test with Welch's correction to determine significance between two conditions/proteins, as described previously (Schmider et al., 2020). Mann–Whitney test analysis was also conducted to validate results (data not shown).

Acknowledgements
We thank the Biological Optical Microscopy Platform, University of Melbourne; the Materials Characterisation and Fabrication Platform, University of Melbourne; the Burnet Cell Imaging Facility, Macfarlane Burnet Institute; and Monash Micro Imaging, Monash University.

Competing interests
The authors declare no competing or financial interests.

Author contributions
Conceptualization: C.S.P., D.S.; Methodology: C.S.P., J.L., E.H.; Software: B.K., E.H.; Formal analysis: J.L., E.P., A.J.A., Y.K., E.H.; Investigation: C.S.P., A.J.A., Y.K.; Resources: B.K., E.P.; Data curation: C.S.P., J.L., B.K., E.P.; Writing - original draft: C.S.P., D.S.; Writing - review & editing: C.S.P., J.L., B.K., E.P., A.J.A., Y.K., D.S.; Visualization: C.S.P.; Supervision: E.H., D.S.; Project administration: D.S.; Funding acquisition: D.S.

Funding
D.S. is supported by the Research Fellowship from the Mito Foundation. We acknowledge funding from the Australian Research Council (ARC) (DP170101249 to D.S.). E.H. and J.L. are supported by grants from the Australian National Health and Medical Research Council (APP1124762 and APP1164000) and the ARC (DP180101387).

Peer review history
The peer review history is available online at https://journals.biologists.com/jcs/article-lookup/doi/10.1242/jcs.252197

References
Anderson, A. J., Jackson, T. D., Stroud, D. A. and Stojanovski, D. (2019). Mitochondria—hubs for regulating cellular biochemistry: emerging concepts and networks. *Open Biol.* **9**, 190126. doi:10.1098/rsob.190126

Appelhans, T. and Busch, K. B. (2017). Dynamic imaging of mitochondrial membrane proteins in specific sub-organelle membrane locations. *Biophys. Rev.* **9**, 345-352. doi:10.1007/s12551-017-0287-1

Appelhans, T., Richter, C. P., Wilkens, V., Hess, S. T., Piehler, J. and Busch, K. B. (2012). Nanoscale organization of mitochondrial microcompartments revealed by combining tracking and localization microscopy. *Nano Lett.* **12**, 610-616. doi:10.1021/nl203343a

Bates, M., Huang, B., Dempsey, G. T. and Zhuang, X. (2007). Multicolor super-resolution imaging with photo-switchable fluorescent probes. *Science* **317**, 1749-1753. doi:10.1126/science.1146598

Bates, M., Jones, S. A. and Zhuang, X. (2013). Stochastic optical reconstruction microscopy (STORM): a method for superresolution fluorescence imaging. *Cold Spring Harb. Protoc.* **2013**, 498-520. doi:10.1101/pdb.top075143

Bausewein, T., Mills, D. J., Langer, J. D., Nitschke, B., Nussberger, S. and Kühlbrandt, W. (2017). Cryo-EM structure of the TOM core complex from Neurospora crassa. *Cell* **170**, 693-700.e7. doi:10.1016/j.cell.2017.07.012

Bausewein, T., Naveed, H., Liang, J. and Nussberger, S. (2020). The structure of the TOM core complex in the mitochondrial outer membrane. *Biol. Chem.* **401**, 687-697. doi:10.1515/hsz-2020-0104

Brown, T. A., Tkachuk, A. N., Shtengel, G., Kopek, B. G., Bogenhagen, D. F., Hess, H. F. and Clayton, D. A. (2011). Superresolution fluorescence imaging of mitochondrial nucleoids reveals their spatial range, limits, and membrane interaction. *Mol. Cell. Biol.* **31**, 4994-5010. doi:10.1128/MCB.05694-11

Chacinska, A., Lind, M., Frazier, A. E., Dudek, J., Meisinger, C., Geissler, A., Sickmann, A., Meyer, H. E., Truscott, K. N., Guiard, B. et al. (2005). Mitochondrial presequence translocase: switching between TOM tethering and motor recruitment involves Tim21 and Tim17. *Cell* **120**, 817-829. doi:10.1016/j.cell.2005.01.011

Chacinska, A., Koehler, C. M., Milenkovic, D., Lithgow, T. and Pfanner, N. (2009). Importing mitochondrial proteins: machineries and mechanisms. *Cell* **138**, 628-644. doi:10.1016/j.cell.2009.08.005

Chacinska, A., van der Laan, M., Mehnert, C. S., Guiard, B., Mick, D. U., Hutu, D. P., Truscott, K. N., Wiedemann, N., Meisinger, C., Pfanner, N. et al. (2010). Distinct forms of mitochondrial TOM-TIM supercomplexes define signal-dependent states of preprotein sorting. *Mol. Cell. Biol.* **30**, 307-318. doi:10.1128/MCB.00749-09

Coelho, S., Baek, J., Graus, M. S., Halstead, J. M., Nicovich, P. R., Feher, K., Gandhi, H., Gooding, J. J. and Gaus, K. (2020). Ultraprecise single-molecule localization microscopy enables in situ distance measurements in intact cells. *Sci. Adv.* **6**, eaay8271. doi:10.1126/sciadv.aay8271

Dlasková, A., Engstová, H., Špaček, T., Kahancová, A., Pavluch, V., Smolková, K., Špačková, J., Bartoš, M., Hlavatá, L. P. and Ježek, P. (2018). 3D super-resolution microscopy reflects mitochondrial cristae alternations and mtDNA nucleoid size and distribution. *Biochim. Biophys. Acta (BBA) Bioenerg.* **1859**, 829-844. doi:10.1016/j.bbabio.2018.04.013

Ester, M., Kriegel, H.-P., Sander, J. and Xu, X. (1996). A density-based algorithm for discovering clusters in large spatial databases with noise. In Proceedings of the Second International Conference on Knowledge Discovery and Data Mining (KDD'96), pp. 226-231. AAAI Press.

Gu, J., Wu, M., Guo, R., Yan, K., Lei, J., Gao, N. and Yang, M. (2016). The architecture of the mammalian respirasome. *Nature* **537**, 639-643. doi:10.1038/nature19359

Guo, R., Zong, S., Wu, M., Gu, J. and Yang, M. (2017). Architecture of human mitochondrial respiratory megacomplex I2III2IV2. *Cell* **170**, 1247-1257.e12. doi:10.1016/j.cell.2017.07.050

Heilemann, M., van de Linde, S., Schuttpelz, M., Kasper, R., Seefeldt, B., Mukherjee, A., Tinnefeld, P. and Sauer, M. (2008). Subdiffraction-resolution fluorescence imaging with conventional fluorescent probes. *Angew. Chem. Int. Ed. Engl.* **47**, 6172-6176. doi:10.1002/anie.200802376

Hock, D. H., Reljic, B., Ang, C.-S., Muellner-Wong, L., Mountford, H. S., Compton, A. G., Ryan, M. T., Thorburn, D. R. and Stroud, D. A. (2020). HIGD2A is required for assembly of the COX3 module of human mitochondrial complex IV. *Mol. Cell. Proteomic.* **19**, 1145-1160. doi:10.1074/mcp.RA120.002076

Huang, B., Jones, S. A., Brandenburg, B. and Zhuang, X. (2008a). Whole-cell 3D STORM reveals interactions between cellular structures with nanometer-scale resolution. *Nat. Methods* **5**, 1047-1052. doi:10.1038/nmeth.1274

Huang, B., Wang, W., Bates, M. and Zhuang, X. (2008b). Three-dimensional super-resolution imaging by stochastic optical reconstruction microscopy. *Science* **319**, 810-813. doi:10.1126/science.1153529

Humphries, A. D., Streimann, I. C., Stojanovski, D., Johnston, A. J., Yano, M., Hoogenraad, N. J. and Ryan, M. T. (2005). Dissection of the mitochondrial import and assembly pathway for human Tom40. *J. Biol. Chem.* **280**, 11535-11543. doi:10.1074/jbc.M413816200

Hutu, D. P., Guiard, B., Chacinska, A., Becker, D., Pfanner, N., Rehling, P. and van der Laan, M. (2008). Mitochondrial protein import motor: differential role of Tim44 in the recruitment of Pam17 and J-complex to the presequence translocase. *Mol. Biol. Cell* **19**, 2642-2649. doi:10.1091/mbc.e07-12-1226

Jackson, T. D., Palmer, C. S. and Stojanovski, D. (2018). Mitochondrial diseases caused by dysfunctional mitochondrial protein import. *Biochem. Soc. Trans.* **46**, 1225-1238. doi:10.1042/BST20180239

Jans, D. C., Wurm, C. A., Riedel, D., Wenzel, D., Stagge, F., Deckers, M., Rehling, P. and Jakobs, S. (2013). STED super-resolution microscopy reveals an array of MINOS clusters along human mitochondria. *Proc. Natl. Acad. Sci. USA* **110**, 8936-8941. doi:10.1073/pnas.1301820110

Kadenbach, B. and Hüttemann, M. (2015). The subunit composition and function of mammalian cytochrome c oxidase. *Mitochondrion* **24**, 64-76. doi:10.1016/j.mito.2015.07.002

Kang, P.-J., Ostermann, J., Shilling, J., Neupert, W., Craig, E. A. and Pfanner, N. (1990). Requirement for hsp70 in the mitochondrial matrix for translocation and folding of precursor proteins. *Nature* **348**, 137-143. doi:10.1038/348137a0

Kang, Y., Stroud, D. A., Baker, M. J., De Souza, D. P., Frazier, A. E., Liem, M., Tull, D., Mathivanan, S., McConville, M. J., Thorburn, D. R. et al. (2017). Sengers syndrome-associated mitochondrial Acylglycerol kinase is a subunit of the human TIM22 protein import complex. *Mol. Cell* **67**, 457-470.e5. doi:10.1016/j.molcel.2017.06.014

Kang, Y., Fielden, L. F. and Stojanovski, D. (2018). Mitochondrial protein transport in health and disease. *Semin. Cell Dev. Biol.* **76**, 142-153. doi:10.1016/j.semcdb.2017.07.028

Kang, Y., Anderson, A. J., Jackson, T. D., Palmer, C. S., De Souza, D. P., Fujihara, K. M., Stait, T., Frazier, A. E., Clemons, N. J., Tull, D. et al. (2019). Function of hTim8a in complex IV assembly in neuronal cells provides insight into pathomechanism underlying Mohr-Tranebjaerg syndrome. *eLife* **8**, e48828. doi:10.7554/eLife.48828

Klotzsch, E., Smorodchenko, A., Löfler, L., Moldzio, R., Parkinson, E., Schütz, G. J. and Pohl, E. E. (2015). Superresolution microscopy reveals spatial separation of UCP4 and F_0F_1-ATP synthase in neuronal mitochondria. *Proc. Natl. Acad. Sci. USA* **112**, 130-135. doi:10.1073/pnas.1415261112

Kühlbrandt, W. (2015). Structure and function of mitochondrial membrane protein complexes. *BMC Biol.* **13**, 89. doi:10.1186/s12915-015-0201-x

Kukat, C., Wurm, C. A., Spahr, H., Falkenberg, M., Larsson, N.-G. and Jakobs, S. (2011). Super-resolution microscopy reveals that mammalian mitochondrial nucleoids have a uniform size and frequently contain a single copy of mtDNA. *Proc. Natl. Acad. Sci. USA* **108**, 13534-13539. doi:10.1073/pnas.1109263108

Lazarou, M., Smith, S. M., Thorburn, D. R., Ryan, M. T. and McKenzie, M. (2009). Assembly of nuclear DNA-encoded subunits into mitochondrial complex IV, and

their preferential integration into supercomplex forms in patient mitochondria. *FEBS J.* **276**, 6701-6713. doi:10.1111/j.1742-4658.2009.07384.x

Lobo-Jarne, T. and Ugalde, C. (2018). Respiratory chain supercomplexes: structures, function and biogenesis. *Semin. Cell Dev. Biol.* **76**, 179-190. doi:10.1016/j.semcdb.2017.07.021

Mannella, C. A., Lederer, W. J. and Jafri, M. S. (2013). The connection between inner membrane topology and mitochondrial function. *J. Mol. Cell. Cardiol.* **62**, 51. doi:10.1016/j.yjmcc.2013.05.001

Mick, D. U., Dennerlein, S., Wiese, H., Reinhold, R., Pacheu-Grau, D., Lorenzi, I., Sasarman, F., Weraarpachai, W., Shoubridge, E. A., Warscheid, B. et al. (2012). MITRAC links mitochondrial protein translocation to respiratory-chain assembly and translational regulation. *Cell* **151**, 1528-1541. doi:10.1016/j.cell.2012.11.053

Model, K., Meisinger, C., Prinz, T., Wiedemann, N., Truscott, K. N., Pfanner, N. and Ryan, M. T. (2001). Multistep assembly of the protein import channel of the mitochondrial outer membrane. *Nat. Struct. Biol.* **8**, 361-370. doi:10.1038/86253

Mokranjac, D. and Neupert, W. (2010). The many faces of the mitochondrial TIM23 complex. *Biochim. Biophys. Acta (BBA) Bioenerg.* **1797**, 1045-1054. doi:10.1016/j.bbabio.2010.01.026

Morgenstern, M., Stiller, S. B., Lubbert, P., Peikert, C. D., Dannenmaier, S., Drepper, F., Weill, U., Höß, P., Feuerstein, R., Gebert, M. et al. (2017). Definition of a high-confidence mitochondrial proteome at quantitative scale. *Cell Rep.* **19**, 2836-2852. doi:10.1016/j.celrep.2017.06.014

Naylor, D. J., Stines, A. P., Hoogenraad, N. J. and Høj, P. B. (1998). Evidence for the existence of distinct mammalian cytosolic, microsomal, and two mitochondrial GrpE-like proteins, the Co-chaperones of specific Hsp70 members. *J. Biol. Chem.* **273**, 21169-21177. doi:10.1074/jbc.273.33.21169

Nunnari, J. and Suomalainen, A. (2012). Mitochondria: in sickness and in health. *Cell* **148**, 1145-1159. doi:10.1016/j.cell.2012.02.035

Oswald, C., Krause-Buchholz, U. and Rödel, G. (2009). Knockdown of human COX17 affects assembly and supramolecular organization of cytochrome c oxidase. *J. Mol. Biol.* **389**, 470-479. doi:10.1016/j.jmb.2009.04.034

Pageon, S. V., Nicovich, P. R., Mollazade, M., Tabarin, T. and Gaus, K. (2016a). Clus-DoC: a combined cluster detection and colocalization analysis for single-molecule localization microscopy data. *Mol. Biol. Cell* **27**, 3627-3636. doi:10.1091/mbc.e16-07-0478

Pageon, S. V., Tabarin, T., Yamamoto, Y., Ma, Y., Nicovich, P. R., Bridgeman, J. S., Cohnen, A., Benzing, C., Gao, Y., Crowther, M. D. et al. (2016b). Functional role of T-cell receptor nanoclusters in signal initiation and antigen discrimination. *Proc. Natl. Acad. Sci. USA* **113**, E5454-E5463. doi:10.1073/pnas.1607436113

Popov-Čeleketić, D., Mapa, K., Neupert, W. and Mokranjac, D. (2008). Active remodelling of the TIM23 complex during translocation of preproteins into mitochondria. *EMBO J.* **27**, 1469-1480. doi:10.1038/emboj.2008.79

Qi, L., Wang, Q., Guan, Z., Wu, Y., Shen, C., Hong, S., Cao, J., Zhang, X., Yan, C. and Yin, P. (2021). Cryo-EM structure of the human mitochondrial translocase TIM22 complex. *Cell Res.* **31**, 369-372. doi:10.1038/s41422-020-00400-w

Rossi, A., Pizzo, P. and Filadi, R. (2019). Calcium, mitochondria and cell metabolism: a functional triangle in bioenergetics. *Biochim. Biophys. Acta (BBA) Mol. Cell Res.* **1866**, 1068-1078. doi:10.1016/j.bbamcr.2018.10.016

Rust, M. J., Bates, M. and Zhuang, X. (2006). Sub-diffraction-limit imaging by stochastic optical reconstruction microscopy (STORM). *Nat. Methods* **3**, 793-796. doi:10.1038/nmeth929

Salewskij, K., Rieger, B., Hager, F., Arroum, T., Duwe, P., Villalta, J., Colgiati, S., Richter, C. P., Psathaki, O. E., Enriquez, J. A. et al. (2020). The spatio-temporal organization of mitochondrial F1FO ATP synthase in cristae depends on its activity mode. *Biochim. Biophys. Acta (BBA) Bioenerg.* **1861**, 148091. doi:10.1016/j.bbabio.2019.148091

Salvador-Gallego, R., Mund, M., Cosentino, K., Schneider, J., Unsay, J., Schraermeyer, U., Engelhardt, J., Ries, J. and García-Sáez, A. J. (2016). Bax assembly into rings and arcs in apoptotic mitochondria is linked to membrane pores. *EMBO J.* **35**, 389-401. doi:10.15252/embj.201593384

Schäfer, E., Seelert, H., Reifschneider, N. H., Krause, F., Dencher, N. A. and Vonck, J. (2006). Architecture of active mammalian respiratory chain supercomplexes. *J. Biol. Chem.* **281**, 15370-15375. doi:10.1074/jbc.M513525200

Schindelin, J., Arganda-Carreras, I., Frise, E., Kaynig, V., Longair, M., Pietzsch, T., Preibisch, S., Rueden, C., Saalfeld, S., Schmid, B. et al. (2012). Fiji: an open-source platform for biological-image analysis. *Nat. Methods* **9**, 676-682. doi:10.1038/nmeth.2019

Schlame, M. (2021). Protein crowding in the inner mitochondrial membrane. *Biochim. Biophys. Acta (BBA) Bioenerg.* **1862**, 148305. doi:10.1016/j.bbabio.2020.148305

Schmider, A. B., Bauer, N. C., Sunwoo, H., Godin, M. D., Ellis, G. E., Lee, J. T., Nigrovic, P. A. and Soberman, R. J. (2020). Two- and three-color STORM analysis reveals higher-order assembly of leukotriene synthetic complexes on the nuclear envelope of murine neutrophils. *J. Biol. Chem.* **295**, 5761-5770. doi:10.1074/jbc.RA119.012069

Sinha, D., Joshi, N., Chittoor, B., Samji, P. and D'Silva, P. (2010). Role of Magmas in protein transport and human mitochondria biogenesis. *Hum. Mol. Genet.* **19**, 1248-1262. doi:10.1093/hmg/ddq002

Sinha, D., Srivastava, S., Krishna, L. and D'Silva, P. (2014). Unraveling the intricate organization of mammalian mitochondrial presequence translocases: existence of multiple translocases for maintenance of mitochondrial function. *Mol. Cell. Biol.* **34**, 1757-1775. doi:10.1128/MCB.01527-13

Stoldt, S., Wenzel, D., Kehrein, K., Riedel, D., Ott, M. and Jakobs, S. (2018). Spatial orchestration of mitochondrial translation and OXPHOS complex assembly. *Nat. Cell Biol.* **20**, 528-534. doi:10.1038/s41556-018-0090-7

Stoldt, S., Stephan, T., Jans, D. C., Brüser, C., Lange, F., Keller-Findeisen, J., Riedel, D., Hell, S. W. and Jakobs, S. (2019). Mic60 exhibits a coordinated clustered distribution along and across yeast and mammalian mitochondria. *Proc. Natl. Acad. Sci. USA* **116**, 9853-9858. doi:10.1073/pnas.1820364116

Stroud, D. A., Maher, M. J., Lindau, C., Vögtle, F.-N., Frazier, A. E., Surgenor, E., Mountford, H., Singh, A. P., Bonas, M., Oeljeklaus, S. et al. (2015). COA6 is a mitochondrial complex IV assembly factor critical for biogenesis of mtDNA-encoded COX2. *Hum. Mol. Genet.* **24**, 5404-5415. doi:10.1093/hmg/ddv265

Suzuki, H., Okazawa, Y., Komiya, T., Saeki, K., Mekada, E., Kitada, S., Ito, A. and Mihara, K. (2000). Characterization of rat TOM40, a central component of the preprotein translocase of the mitochondrial outer membrane. *J. Biol. Chem.* **275**, 37930-37936. doi:10.1074/jbc.M006558200

Tam, J. and Merino, D. (2015). Stochastic optical reconstruction microscopy (STORM) in comparison with stimulated emission depletion (STED) and other imaging methods. *J. Neurochem.* **135**, 643-658. doi:10.1111/jnc.13257

Tam, J., Cordier, G. A., Borbely, J. S., Sandoval Álvarez, A. and Lakadamyali, M. (2014). Cross-talk-free multi-color STORM imaging using a single fluorophore. *PLoS ONE* **9**, e101772. doi:10.1371/journal.pone.0101772

Timón-Gómez, A., Garlich, J., Stuart, R. A., Ugalde, C. and Barrientos, A. (2020). Distinct roles of mitochondrial HIGD1A and HIGD2A in respiratory complex and supercomplex biogenesis. *Cell Rep.* **31**, 107607. doi:10.1016/j.celrep.2020.107607

van de Linde, S., Sauer, M. and Heilemann, M. (2008). Subdiffraction-resolution fluorescence imaging of proteins in the mitochondrial inner membrane with photoswitchable fluorophores. *J. Struct. Biol.* **164**, 250-254. doi:10.1016/j.jsb.2008.08.002

van der Laan, M., Meinecke, M., Dudek, J., Hutu, D. P., Lind, M., Perschil, I., Guiard, B., Wagner, R., Pfanner, N. and Rehling, P. (2007). Motor-free mitochondrial presequence translocase drives membrane integration of preproteins. *Nat. Cell Biol.* **9**, 1152-1159. doi:10.1038/ncb1635

van der Laan, M., Horvath, S. E. and Pfanner, N. (2016). Mitochondrial contact site and cristae organizing system. *Curr. Opin. Cell Biol.* **41**, 33-42. doi:10.1016/j.ceb.2016.03.013

Vögtle, F.-N., Burkhart, J. M., Gonczarowska-Jorge, H., Kücükköse, C., Taskin, A. A., Kopczynski, D., Ahrends, R., Mossmann, D., Sickmann, A., Zahedi, R. P. et al. (2017). Landscape of submitochondrial protein distribution. *Nat. Commun.* **8**, 290. doi:10.1038/s41467-017-00359-0

Wilkens, V., Kohl, W. and Busch, K. (2013). Restricted diffusion of OXPHOS complexes in dynamic mitochondria delays their exchange between cristae and engenders a transitory mosaic distribution. *J. Cell Sci.* **126**, 103-116. doi:10.1242/jcs.108852

Wu, M., Gu, J., Guo, R., Huang, Y. and Yang, M. (2016). Structure of mammalian respiratory supercomplex $I_1III_2IV_1$. *Cell* **167**, 1598-1609.e10. doi:10.1016/j.cell.2016.11.012

Wurm, C. A., Neumann, D., Lauterbach, M. A., Harke, B., Egner, A., Hell, S. W. and Jakobs, S. (2011). Nanoscale distribution of mitochondrial import receptor Tom20 is adjusted to cellular conditions and exhibits an inner-cellular gradient. *Proc. Natl. Acad. Sci. USA* **108**, 13546-13551. doi:10.1073/pnas.1107553108

Zhao, R.-Z., Jiang, S., Zhang, L. and Yu, Z.-B. (2019). Mitochondrial electron transport chain, ROS generation and uncoupling (Review). *Int. J. Mol. Med.* **44**, 3-15. doi:10.3892/ijmm.2019.4188

Zick, M., Rabl, R. and Reichert, A. S. (2009). Cristae formation—linking ultrastructure and function of mitochondria. *Biochim. Biophys. Acta (BBA) Mol. Cell Res.* **1793**, 5-19. doi:10.1016/j.bbamcr.2008.06.013

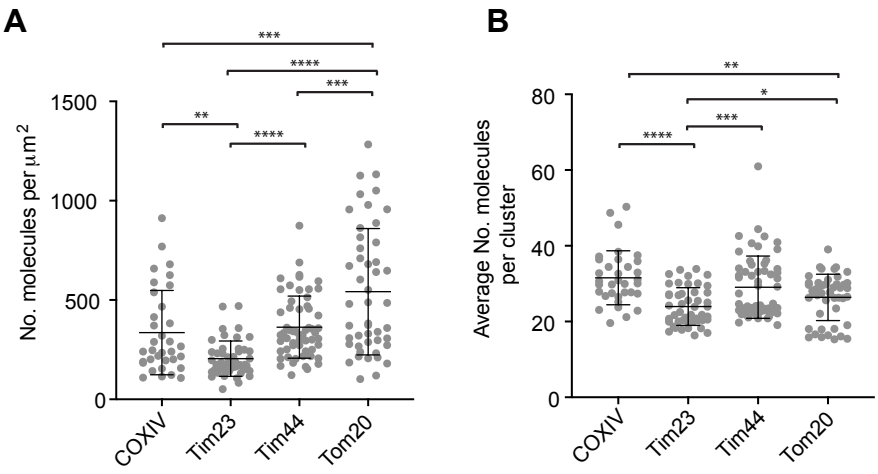

Fig. S1. Mitochondrial inner and outer membrane proteins have distinct numbers of molecules per μm². Representative regions of 4×4 μm² from N-STORM single molecule localisation data were analysed for cluster properties by cluster analysis program DBSCAN for COXIV, Tim23, Tim44 and Tom20. (A) The number of molecules per μm² of selected regions from single molecule localisation. (B) The average number of molecules per cluster selected regions from single molecule localisation. n = 3 experiments, ≥ 33 regions from ≥ 9 cells per protein examined. Data are mean ± s.d.; **P* < 0.05, ***P* < 0.01, ****P* < 0.001, *****P* < 0.0001 (unpaired *t* test with Welch's correction).

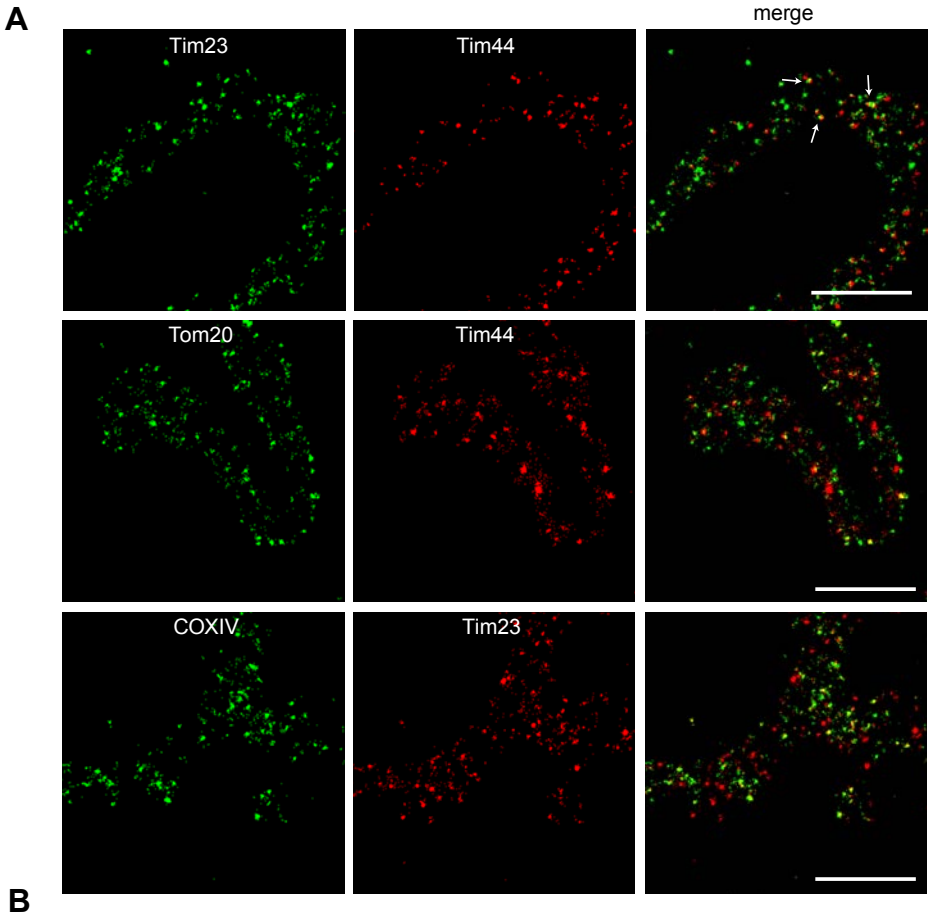

Fig. S2. Two colour STORM microscopy reveals arrangement of TIM23 complexes. (A) Schematic of the known TIM23 complex formations, with the Tim23 protein present in two distinct molecular machineries: the $TIM23^{SORT}$ complex and the $TIM23^{MOTOR}$ complex. (B) HeLa cells were immunostained for the proteins Tim23 and Tim44 (upper), Tom20 and Tim44 (middle) or COXIV and Tim23 (bottom) and visualised by STORM microscopy. Representative regions of STORM reconstructions are shown here. Scale bar = 1 μm. Arrows indicate representative points containing both Tim23 and Tim44.